

Mixed Quantum-Classical Molecular Dynamics Analysis of the Molecular-Level Mechanisms of Vibrational Frequency Shifts

Christine M. Morales and Ward H. Thompson*

Department of Chemistry, University of Kansas, Lawrence, Kansas 66045

Received: February 28, 2007; In Final Form: April 6, 2007

A detailed analysis of the origins of vibrational frequency shifts of diatomic molecules (I_2 and ICl) in a rare gas (Xe) liquid is presented. Specifically, vibrationally adiabatic mixed quantum-classical molecular dynamics simulations are used to obtain the instantaneous frequency shifts and correlate the shifts to solvent configurations. With this approach, important mechanistic questions are addressed, including the following: How many solvent atoms determine the frequency shift? What solvent atom configurations lead to blue shifts, and which lead to red shifts? What is the effect of solute asymmetry? The mechanistic analysis can be generally applied and should be useful in understanding what information is provided by infrared and Raman spectra about the environment of the probed vibrational mode.

1. Introduction

Vibrational spectra of solutes in condensed phases are frequently used as probes of the environment of the active mode(s). The interactions of the solute with its surroundings affect its vibrational frequencies leading to line shifts and line broadening or, in some cases, motional narrowing. To understand what these modifications of the spectral features tell us about the solute environment, it is critical to have a molecular-level picture of the mechanisms of vibrational frequency shifts. Such mechanistic understanding is relevant to an increasing body of research as more complex systems are subjected to study and as the development and application of nonlinear spectroscopic techniques that can probe the frequency autocorrelation function continues.

One motivation for such study is that recently there has been significant interest in the properties of liquids confined on the nanometer length scale. Such nanostructured porous materials have numerous potential applications in catalysis, optical materials, sensing, separations, and biology, and their relevance continues to increase as new synthetic techniques are developed. Infrared and Raman spectroscopy are often used as experimental probes of the structure and dynamics of porous materials, but the factors that determine the spectra in systems with nanoscale structure^{1–22} are not well-established, complicating the interpretation. In particular, the effect of confinement in porous materials such as reverse micelles and sol-gels on the vibrational spectra of liquids have been the subject of a number of studies.^{3,4,11–19,23–26} A better understanding of the molecular-level mechanisms determining the vibrational spectra is needed to fully interpret measured spectra of nanoconfined liquids and solutes dissolved therein. The approaches described in this paper can provide this insight into the mechanisms by allowing the assignment of the solvent structural arrangements and motions that give rise to vibrational line shifts and dephasing.

Specifically, we present a number of methods for analyzing the results of vibrationally adiabatic mixed quantum-classical molecular dynamics (MD) simulations.²⁷ These simulations allow feedback between the solute and solvent by allowing the

solute vibrational wavefunction to influence the solvent atom dynamics and vice versa. Moreover, the mixed quantum-classical approach provides extremely accurate instantaneous frequency shifts^{27–29} and allows those frequency shifts to be connected with the solvent positions and dynamics. As has been demonstrated previously, careful analysis of mixed quantum-classical trajectory information can lead to deep insights about the mechanistic origins of vibrational frequency shifts in a liquid^{29,30} and analogously, for vibrational relaxation as well.³¹

In this paper, we illustrate these approaches by application to two test systems, I_2 or ICl in liquid Xe. These provide useful illustrations of the mechanistic information that can be extracted, simplified by the single vibrational mode and the atomic solvent; the comparison of a symmetric and an asymmetric solute is also interesting. The vibrational spectral and relaxation properties of I_2 in Xe have been extensively studied experimentally^{32,33} and theoretically,^{34–44} with most of the work focusing on the vibrational relaxation of highly excited I_2 in Xe at different temperatures and densities. The vibrational energy decay was found to scale linearly along the time axis at different temperatures and densities,^{32–34} consistent with the “isolated binary collision” (IBC) model.^{45–48} This model is frequently used to describe vibrational frequency shifts and energy transfer in liquids as well as dense gases (although a physical definition for a “collision” can be problematic in a liquid). In a recent study, Larsen and Stratt⁴¹ were able to recover the short-time dynamics of vibrational relaxation for I_2 in Xe using an instantaneous normal-mode analysis based on binary interactions between solute–solvent pairs that are mutual nearest-neighbors. Their work indicated that these binary contributions to the rate are much more important than the corresponding ternary contributions from interactions between a solute and two solvent atoms. Li and Thompson^{29,31} found, using mixed quantum-classical simulations with analogous, but cruder, analysis techniques to those presented here, that more than one solvent atom is involved in the relaxation, but only a few atoms participate significantly; the microscopic picture obtained was consistent with the presence of solute–solvent “collisions” implicit in the IBC model but contradicted the notion that they were isolated or binary. Further, they found that the leading

* Corresponding author.

contributions come from solvent atoms that are either near the ends of the I₂ molecule or very close to the center.

The remainder of the paper is organized as follows. The mixed quantum-classical molecular dynamics approach for simulating the frequency shifts and determining the contributions of each solvent atom is described in section 2. The results of the simulations are presented in section 3, where the origin of the vibrational line shift distribution is examined using a number of analysis tools. Finally, some concluding remarks are given in section 4.

2. Methods

2.1. Theory. We have used vibrationally adiabatic, mixed quantum-classical simulations to analyze the microscopic origins of frequency shifts of I₂ in liquid Xe. This approach has been described in full detail elsewhere;²⁷ here, we discuss the relevant features. The full classical Hamiltonian for the system can be written as follows:

$$H(r, p_r, \mathbf{e}, \mathbf{p}_e, \mathbf{Q}, \mathbf{P}) = \frac{p_r^2}{2\mu} + \frac{\mathbf{p}_e^2}{2\mu r^2} + \sum_{j=2}^N \frac{\mathbf{P}_j^2}{2m_j} + V(r, \mathbf{e}, \mathbf{Q}) \quad (1)$$

where r and \mathbf{e} are the bond distance and orientation coordinates of the diatomic solute with corresponding momenta p_r and \mathbf{p}_e , $\mathbf{Q} = (\mathbf{Q}_1, \mathbf{Q}_2, \dots, \mathbf{Q}_N)$ are the coordinates of the solute center-of-mass and $N-1$ solvent atoms with corresponding momenta $\mathbf{P} = (\mathbf{P}_1, \mathbf{P}_2, \dots, \mathbf{P}_N)$, μ is the solute reduced mass, and m_j is the mass of solvent atom j . The potential energy, $V(r, \mathbf{e}, \mathbf{Q})$, is described using a Morse potential for the I₂ bond distance r plus pairwise Lennard–Jones potentials for all solute–solvent and solvent–solvent interactions. We impose a mixed quantum-classical adiabatic approximation for the I₂ vibration, in which the “fast” solute vibration is described quantum-mechanically while all other degrees of freedom are governed by classical equations of motion. The quantum mechanical Hamiltonian \hat{h}_r is as follows for a given set of center-of-mass positions and momenta:

$$\hat{h}_r(\mathbf{e}, \mathbf{p}_e, \mathbf{Q}) = \frac{\hat{p}_r^2}{2\mu} + \frac{\mathbf{p}_e^2}{2\mu r^2} + \hat{V}(\hat{r}; \mathbf{e}, \mathbf{p}_e, \mathbf{Q}) \quad (2)$$

For fixed values of the classical variables, \mathbf{e} , \mathbf{p}_e , and \mathbf{Q} , the vibrational Schrödinger equation is solved for the adiabatic vibrational states, ϕ_n , and corresponding energies, E_n :

$$\hat{h}_r(\mathbf{e}, \mathbf{p}_e, \mathbf{Q})\phi_n(r; \mathbf{e}, \mathbf{p}_e, \mathbf{Q}) = E_n(\mathbf{e}, \mathbf{p}_e, \mathbf{Q})\phi_n(r; \mathbf{e}, \mathbf{p}_e, \mathbf{Q}) \quad (3)$$

These solutions depend implicitly on time through the changes in the classical variables \mathbf{e} , \mathbf{p}_e , and \mathbf{Q} . A vibrationally adiabatic Hamiltonian is then generated with the solved eigenfunction and energy level for state n ,

$$\begin{aligned} H_n(\mathbf{e}, \mathbf{p}_e, \mathbf{Q}, \mathbf{P}) &= \sum_{j=2}^N \frac{\mathbf{P}_j^2}{2m_j} + \langle \phi_n | \hat{h}_r | \phi_n \rangle_r \\ &= \sum_{j=2}^N \frac{\mathbf{P}_j^2}{2m_j} + E_n(\mathbf{e}, \mathbf{p}_e, \mathbf{Q}) \end{aligned} \quad (4)$$

which determines the equations of motion for the classical variables. In the present work, the classical trajectory is propagated in the ground state, $n = 0$. It is important to note

that in this approach the solute vibrational wavefunction influences the solvent dynamics just as the solvent dynamics influence the solute vibrational wavefunction.

The vibrational line shifts at each time step can be decomposed into contributions from particular solute–solvent interactions to provide detailed insight into the mechanism of the shifts. The present study focuses on solvent configurations that give rise to a distribution of fundamental frequencies $\omega_{01} = \Delta E_{01}/\hbar$. The transition energy between any two states m and n consists of the differences in the kinetic energy and the potential terms between m and n :

$$\begin{aligned} \Delta E_{mn}(\mathbf{e}, \mathbf{p}_e, \mathbf{Q}) &= E_m(\mathbf{e}, \mathbf{p}_e, \mathbf{Q}) - E_n(\mathbf{e}, \mathbf{p}_e, \mathbf{Q}) \\ &= \left\langle \phi_m \left| \frac{\hat{p}_r^2}{2\mu} \right| \phi_m \right\rangle_r - \left\langle \phi_n \left| \frac{\hat{p}_r^2}{2\mu} \right| \phi_n \right\rangle_r + \\ &\quad \left\langle \phi_m \left| \frac{\mathbf{p}_e^2}{2\mu \hat{r}^2} \right| \phi_m \right\rangle_r - \left\langle \phi_n \left| \frac{\mathbf{p}_e^2}{2\mu \hat{r}^2} \right| \phi_n \right\rangle_r + \\ &\quad \langle \phi_m | \hat{V}_{AB}(\hat{r}) | \phi_m \rangle_r - \langle \phi_n | \hat{V}_{AB}(\hat{r}) | \phi_n \rangle_r + \\ &\quad \sum_{\alpha=A}^B \sum_{\alpha=j=2}^N [\langle \phi_m | \hat{V}_{\alpha j}(r_{\alpha j}) | \phi_m \rangle_r - \langle \phi_n | \hat{V}_{\alpha j}(r_{\alpha j}) | \phi_n \rangle_r] \end{aligned} \quad (5)$$

$$\begin{aligned} \Delta E_{mn}(\mathbf{e}, \mathbf{p}_e, \mathbf{Q}) &= \Delta T_{mn}^r(\mathbf{e}, \mathbf{p}_e, \mathbf{Q}) + \Delta T_{mn}^e(\mathbf{e}, \mathbf{p}_e, \mathbf{Q}) + \\ &\quad \Delta V_{mn}^{AB}(\mathbf{e}, \mathbf{p}_e, \mathbf{Q}) + \sum_{j=2}^N \Delta V_{mn}^{(j)}(\mathbf{e}, \mathbf{p}_e, \mathbf{Q}) \end{aligned} \quad (6)$$

where

$$\Delta V_{mn}^{(j)}(\mathbf{e}, \mathbf{p}_e, \mathbf{Q}) \equiv \sum_{\alpha=A}^B [\langle \phi_m | \hat{V}_{\alpha j}(\hat{r}_{\alpha j}) | \phi_m \rangle_r - \langle \phi_n | \hat{V}_{\alpha j}(\hat{r}_{\alpha j}) | \phi_n \rangle_r]$$

Here, $\hat{V}_{\alpha j}(r)$ is the pairwise interatomic potential between atom α and atom j . Note that solvent atom j interacts with the two solute atoms, A and B , through the solute–solvent potential terms, $\hat{V}_{Aj}(r_{\alpha j})$ and $\hat{V}_{Bj}(r_{\alpha j})$. Because solute–solvent interactions are modeled by a pairwise additive potential, their contributions $\Delta V_{mn}^{(j)}$ to the transition energy are additive. The $\Delta V_{mn}^{(j)}$ contributions depend explicitly on solvent coordinates \mathbf{Q}_j and the solute orientation \mathbf{e} . In addition, it and remaining terms vary with \mathbf{e} , \mathbf{p}_e , and \mathbf{Q} through implicit dependence on ϕ_m and ϕ_n . Such implicit solvent effects cannot be decomposed into a sum over pairwise solute–solvent interactions, but can be shown to have the same sign for the most part as $\sum_{j=2}^N \Delta V_{mn}^{(j)}$. The energy gap ΔE_{mn} can also be expressed in terms of vibrational line shifts $\Delta\omega_{mn}$, relative to the gas-phase frequency:

$$\begin{aligned} \Delta\omega_{mn} &= [\Delta E_{mn}^{\text{solv}} - \Delta E_{mn}^{\text{gas}}]/\hbar = [\{\Delta T_{mn}^r - \Delta T_{mn}^r(\text{gas})\} + \\ &\quad \Delta T_{mn}^e + \{\Delta \hat{V}_{mn}^{AB} - \Delta \hat{V}_{mn}^{AB}(\text{gas})\} + \sum_{j=2}^N \Delta V_{mn}^{(j)}]/\hbar \end{aligned} \quad (7)$$

$$\Delta\omega_{mn} = \Delta\omega_{mn}^{(0)} + \left[\sum_{j=2}^N \Delta V_{mn}^{(j)} \right] / \hbar \quad (8)$$

where

$$\begin{aligned} \Delta\omega_{mn}^{(0)} &= [\{\Delta T_{mn}^r - \Delta T_{mn}^r(\text{gas})\} + \Delta T_{mn}^e + \\ &\quad \{\Delta \hat{V}_{mn}^{AB}(r) - \Delta \hat{V}_{mn}^{AB}(r)(\text{gas})\}]/\hbar \end{aligned}$$

Solute–solvent potential terms $\Delta V_{01}^{(j)}/\hbar$ remain pairwise addi-

TABLE 1: Potential Parameters

		I–Xe	Cl–Xe	Xe–Xe	I–I	I–Cl
Lennard–Jones ⁴⁹	σ (Å)	3.94	3.73	4.10		
	ϵ (K)	323.7	196.1	221.6		
	D_e (eV)				1.547	2.152
Morse ⁵⁰	α (Å ⁻¹)				1.864	1.860
	r_0 (Å)				2.667	2.321

tive; the other terms that depend implicitly on \mathbf{e} , \mathbf{p}_e , and \mathbf{Q} are grouped together as $\Delta\omega_{mn}^{(0)}$. Upon analyzing these contributions, we can gain insight into the mechanism.

2.2. Simulation Details. In this work, a single solute molecule was simulated within a solvent of 255 Xe atoms. Standard Lennard–Jones parameters were used to describe solute–solvent and solvent–solvent interactions.⁴⁹ The intramolecular I₂ interaction was described by a Morse potential.⁵⁰ Potential parameters are summarized in Table 1.

The solution was modeled at a density of 2.5 g/cm³ or $\rho^* = \rho/\sigma_{\text{Xe}}^3 = 0.79$ in a cubic box of length 28.16 Å. Periodic boundary conditions with the minimum image convention were used.⁴⁹ At a simulation temperature of 244 K, trajectories were generated using constant energy (NVE) molecular dynamics with velocity rescaling during the initial classical equilibration and the first 10 ps of the mixed quantum-classical equilibration stage. Twelve trajectories in the $n = 0$ ground state were propagated for each solute considered. For the purpose of efficiency, only the lowest three vibrational states are included when diagonalizing the quantum Hamiltonian to solve the vibrational Schrödinger equation at each time step. Each trajectory consisted of a classical warm-up stage of 750–887.5 ps with time steps of 2.5 fs, followed by a mixed quantum-classical warm-up stage of 100 ps with time steps of 1 fs and a 2 ns data collection stage with a time step of 1 fs. The reported mean and variance for each variable of interest was obtained by simple block averaging over 12 trajectories. Error bars were calculated at a 95% confidence level using the student t distribution.^{51,52}

3. Results and Discussion

When a solute is placed in solution, dynamic fluctuations in the intermolecular interactions with the solvent modify the solute vibrational frequencies; that is, there is spectral diffusion. The vibrational frequency fluctuations determine the line shape in the infrared or Raman spectra. Further, nonlinear spectroscopic techniques can probe the spectral diffusion relatively directly in a number of systems. While these spectroscopic properties provide insight into the environment of the solute, a microscopic physical picture often must be inferred rather than obtained directly. The present simulations offer a direct, atomic-level view of the origins of the spectral diffusion of the fundamental vibrational transitions of dilute I₂ and ICl in liquid Xe. To elucidate the mechanism by which asymmetry in the ICl molecule leads to changes in the vibrational spectrum, simulations were also carried out for two alchemical mutations of the ICl molecule, one in which the I mass is used for both atoms and another in which the I and Cl Lennard–Jones parameters are switched.

3.1. Distribution of Vibrational Line Shifts. A key way to view the effect of solvent interactions on the solute vibration is through the normalized distribution $P(\Delta\omega)$ of instantaneous vibrational line shifts $\Delta\omega$. This distribution was calculated for each solute from the simulations described in section 2.2, and the results are shown in Figure 1. In Table 2, the values of the average frequency $\langle\omega\rangle$ relative to the gas-phase frequency ω_0 ,

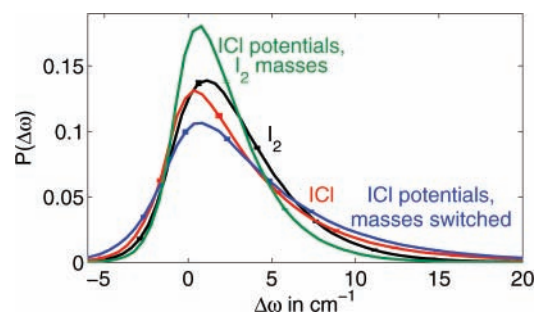


Figure 1. Normalized distribution of instantaneous fundamental vibrational line shifts relative to the gas-phase frequency ω_0 for I₂, ICl, and two fictitious solutes: I₂ with the potential parameters of ICl and ICl with the potential parameters reversed. Error bars, shown at selected intervals, represent a 95% confidence level. All simulations were carried out in Xe at 244 K, $\rho = 2.5$ g/cm³.

TABLE 2: Calculated 0 → 1 Vibrational Frequencies (in cm⁻¹) in the Gas Phase and in Liquid Xe

system	gas phase ω_0	solvated $\langle\omega\rangle - \omega_0$	solvated $\sqrt{\langle(\omega - \omega_0)^2\rangle}$
I ₂	212.4	2.7	3.5
ICl	380.0	3.4	5.0
I ₂ with ICl potentials	250.8	2.1	2.8
ICl with potentials reversed	380.0	3.8	5.6

and the root-mean-square fluctuation, $\sqrt{\langle(\omega - \omega_0)^2\rangle}$, are given. The simulations show both I₂ and ICl blue shifted by about 3 cm⁻¹ in liquid Xe relative to the gas phase. The ICl frequency is slightly more blue shifted, $\langle\omega\rangle - \omega_0 = 3.4$ cm⁻¹, than that of I₂ at 2.7 cm⁻¹. Further, the width of the distribution of frequencies, as measured by $\sqrt{\langle(\omega - \omega_0)^2\rangle}$, is greater for ICl (5.0 cm⁻¹) than for I₂ (3.5 cm⁻¹). These effects can be seen in Figure 1, where the normalized distribution of ICl line shifts is compared to that of I₂. The ICl distribution has a comparatively long tail on the blue-shifted side ($\Delta\omega = \omega - \omega_0 > 0$). It is this blue-shifted tail that accounts for a broader standard deviation and for a slightly larger average line shift. In other words, the asymmetric ICl molecule experiences a greater percentage of strong blue-shifting interactions with the liquid Xe solvent than does the symmetric I₂.

The distributions of frequencies for the two fictitious solutes mentioned above give some indication of the mechanistic origin of stronger ICl frequency shifts in liquid Xe. First, a solute with the atomic masses of I₂ was modified by using potential parameters appropriate for ICl. In simulations using this solute, the distribution of vibrational line shifts is narrower than that of I₂, with $\sqrt{\langle(\omega - \omega_0)^2\rangle} = 2.8$ cm⁻¹. Further, the average line shift is 2.1 cm⁻¹ compared with 2.7 cm⁻¹ for I₂, indicating that strong blue-shifting interactions are less prevalent; this is confirmed by an examination of the distribution plotted in Figure 1 in which the blue-shifted tail is less extensive for this fictitious solute than for I₂. This suggests that the lighter mass of the Cl atom, not its smaller size, is responsible for an increased percentage of strongly blue-shifting ICl–solvent interactions. In addition, a smaller atomic radius appears to reduce the incidence of strongly blue-shifting interactions, possibly by reducing the “collisional” cross section. This can also be seen from the results for the second fictitious solute, for which the atomic masses are the same as ICl but the I and Cl potential parameters are switched. For this solute, the distribution of line shifts is even broader than for ICl, with $\sqrt{\langle(\omega - \omega_0)^2\rangle} = 5.6$ cm⁻¹, and the average line shift is more blue shifted with $\langle\omega\rangle - \omega_0 = 3.8$ cm⁻¹. From Figure 1, it is clear that the blue-shifted

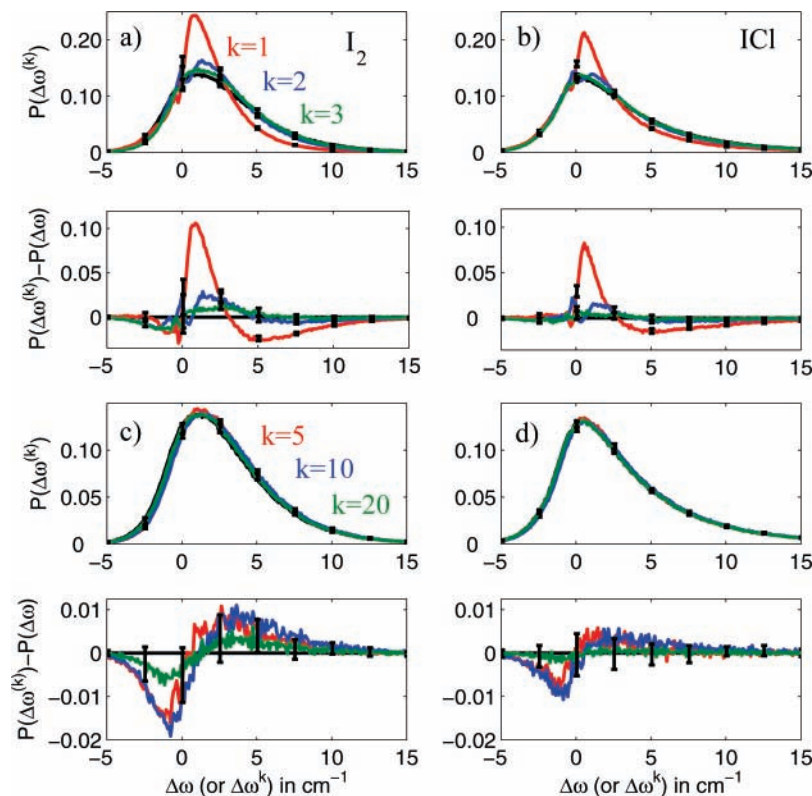


Figure 2. Normalized frequency distribution of total line shifts and truncated sums, see eq 10, representing contributions from the k strongest interactions: (a) I_2 line shifts for $k = 1, 2,$ and 3 ; (b) ICI line shifts for $k = 1, 2,$ and 3 ; (c) I_2 line shifts for $k = 5, 10,$ and 20 ; (d) ICI line shifts for $k = 5, 10,$ and 20 . Distributions $P(\Delta\omega)$ of total line shifts are shown in black, while distributions of truncated sums $P(\Delta\omega^{(k)})$, which only take into account the top k contributions, are shown in red ($k = 1, 5$), blue ($k = 2, 10$), and green ($k = 3, 20$). Also shown are the residuals, $P(\Delta\omega^{(k)}) - P(\Delta\omega)$. Error bars are displayed in black at intervals, except on the residuals for $k = 5$ and 10 . Errors on the residuals for $k = 5$ and 10 are similar to those on the residuals for $k = 20$.

tail of the distribution of frequencies for this fictitious solute extends further than that of ICI. Thus, the increase in strong blue-shifting interactions coincides with an increase in the size of the lighter atom relative to that of the heavier solute atom. These comparisons hint that the solvent configurations leading to the largest blue shifts involve interactions with the lighter end of the asymmetric solute molecules.

3.2. Solvent Atom Contributions to Vibrational Line Shifts. In this section, we address the important question: How many solvent atoms are involved in determining the line shift? As described in section 2.1, at each time step in the vibrationally adiabatic mixed quantum-classical simulation, the instantaneous line shift in the fundamental frequency, $\Delta\omega = \omega - \omega_0$, is calculated. Contributions to $\Delta\omega$ that depend explicitly on individual solute–solvent interactions are then given by $\Delta V_{01}^{(j)}/\hbar$. These were calculated for each Xe atom at every tenth time step and ranked in descending order:

$$\Delta V_{01}^{(\text{Rank}1)} \geq \Delta V_{01}^{(\text{Rank}2)} \geq \dots \geq \Delta V_{01}^{(\text{Rank} N-1)} \quad (9)$$

The sum over Xe atoms in the line shift expression, eq 8, can then be truncated to include only the k largest contributions $\Delta V_{01}^{(j)}/\hbar$, as follows:

$$\Delta\omega^{(k)} = \Delta\omega_{01}^{(0)} + \left[\sum_{i=1}^k \Delta V_{01}^{(\text{Rank} i)} \right] / \hbar \quad (10)$$

where

$$k \leq N - 1$$

It should be noted that the full, implicit solvent effect on $\Delta\omega_{01}^{(0)}$ through changes in ϕ_0 and ϕ_1 is retained. Figure S1 in Supporting Information shows how these implicit solvent effects vary with I_2 and ICI line shifts. The kinetic (ΔT_{01}^r) and Morse potential ($\Delta \hat{V}_{01}^{AB}$) terms along the vibrating degree of freedom increase relative to their gas-phase values as the solute vibration is blue shifted. This is due to a decrease in $\langle \hat{r} \rangle$ relative to the gas-phase equilibrium bond distance r_{eq} , and results in a small enhancement of instantaneous, solvent-induced vibrational blue shifts. The rotational kinetic energy term (ΔT_{01}^e), not present in the gas phase, leads to a negative (red shifting) contribution. This term is small when $\langle \hat{r} \rangle$ is less than r_{eq} but takes on larger negative values as $\langle \hat{r} \rangle$ increases beyond r_{eq} . The extent to which ΔT_{01}^e enhances solvent-induced vibrational red shifts also depends on the rotational momentum \mathbf{p}_e . Notably, $\Delta\omega_{01}^{(0)}$ increases monotonically with the vibrational line shift and is only slightly negative for $\Delta\omega \sim 0 \text{ cm}^{-1}$. As a result, the truncated line shifts $\Delta\omega^{(k)}$ vary in the same direction as the additive terms $\sum_{i=1}^k \Delta V_{01}^{(\text{Rank} i)}/\hbar$, which also determine the sign of the line shift except for a small offset near zero.

Clearly, $\Delta\omega^{(k)}$ converges to the total line shift as $k \rightarrow N - 1$. The rapidity of the convergence is a measure of the number of solvent atoms determining the line shift. We note that at the simulation density of 2.5 g/cm^3 , on average, less than 50 solvent atoms are found within the Lennard–Jones cutoff radius of 10 \AA . Distributions $P(\Delta\omega^{(k)})$ of the truncated line shifts from simulations on I_2 and ICI solutes are plotted for $k = 1, 2, 3, 5, 10,$ and 20 in Figure 2 and are compared with the total vibrational line shift distribution. Figure 2 also shows residuals

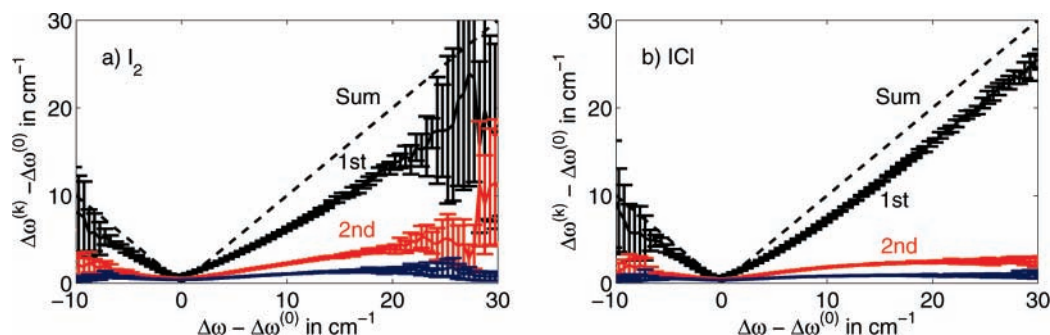


Figure 3. Three largest average absolute contributions of Xe atoms to the line shift, as given by eq 11, vs the sum of solute–solvent contributions to (a) I_2 and (b) ICl line shifts. Dashed lines represent the sum of solute–solvent contributions.

that are obtained by subtracting the total distribution, $P(\Delta\omega)$, from $P(\Delta\omega^{(k)})$.

By showing the significance of successive solvent atom contributions to the solute line shift, this approach relates the full MD results to simplified models of vibrational dynamics such as the isolated binary collision (IBC) model. If the distribution of values for the first truncated expression, $\Delta\omega^{(1)}$, closely approximates the distribution of total line shifts, $\Delta\omega$, then the IBC model is accurate; that is, the single strongest instantaneous solute–solvent potential contribution is sufficient. More generally, residual differences between the distribution of the k th truncated expression and that of the total allow a quantitative analysis of the systematic error incurred when spectral diffusion is attributed to a limited number of solute–solvent interactions.

Interestingly, the distribution of $\Delta\omega^{(1)}$ is quite different from the total distribution. As shown by the red curves in Figure 2a,b, the blue-shifted ($\Delta\omega^{(k)} > 0$) and red-shifted ($\Delta\omega^{(k)} < 0$) branches are separated by a jagged discontinuity in the distribution. This is due to the vanishing number of individual contributions, $\Delta V_{01}^1/\hbar$, that are both exactly equal to zero and simultaneously the largest solute–solvent potential contribution to the line shift.⁵³ On the blue-shifted side, the distribution of truncated sums, $\Delta\omega^{(1)}$, is narrower than that of the total line shifts, $\Delta\omega$. This shows that the cumulative effects of multiple solute–solvent interactions are necessary to explain many of the strongest blue shifts. The difference between the distribution of $\Delta\omega^{(1)}$ and that of $\Delta\omega$ can also be seen in the residuals, plotted below the distributions in Figure 2. Residuals clarify the deficit in the blue-shifted tail, beginning at $\Delta\omega^{(1)} \approx 3 \text{ cm}^{-1}$ for I_2 and at $\Delta\omega^{(1)} \approx 2.5 \text{ cm}^{-1}$ for ICl. This deficit is naturally compensated by an increased population of smaller blue shifts since both distributions are normalized. The residuals are larger for I_2 than for ICl, indicating that an isolated binary collision model is more accurate for the asymmetric ICl solute than for I_2 . Tellingly, the maximum of the $P(\Delta\omega^{(1)}) - P(\Delta\omega)$ residual is nearly as large as that of $P(\Delta\omega)$ itself, even for ICl. This shows the limitations of a model based on isolated binary solute–solvent interactions for the distribution of vibrational line shifts, even for systems dominated by short-range interactions.

Given that the distribution of line shifts is not the result of strictly binary and isolated interactions, we next consider the combined effect of a few strong collisions on the line shift. As illustrated in Figure 2a,b (top panels), the distributions $P(\Delta\omega^{(k)})$ clearly are in closer agreement with the total distributions, $P(\Delta\omega)$, as k increases. The nature of these successive improvements is seen in the residuals, $P(\Delta\omega^{(k)}) - P(\Delta\omega)$ (below top panels). Whereas the residuals $P(\Delta\omega^{(1)}) - P(\Delta\omega)$ clearly show a deficit of strong blue shifts and an excess of weak blue shifts,

the residuals $P(\Delta\omega^{(3)}) - P(\Delta\omega)$ for strong blue shifts are indistinguishable from zero within statistical error. This shows that strong blue shifts can be attributed to simultaneous contributions from only two or three Xe atoms. However, the residuals also reveal that there are fewer strong red shifts in the distributions $P(\Delta\omega^{(3)})$ for I_2 and ICl than for $P(\Delta\omega^{(1)})$. For I_2 , the residuals $P(\Delta\omega^{(3)}) - P(\Delta\omega)$ show a deficit of red shifts. In this case, the distribution of vibrational red shifts is better described by an “isolated, binary” model than by an expanded model with a few strong interactions; however, in addition to the simple “collisional” physical picture, these red shifts also depend on the approach geometry (see section 3.3).

With additional contributions to the I_2 and ICl vibrational line shifts, the distributions $P(\Delta\omega^{(k)})$ converge toward $P(\Delta\omega)$ as shown in Figure 2c,d. The peaks of the distributions $P(\Delta\omega)$ are better described by $P(\Delta\omega^{(10)})$ (blue curves) and $P(\Delta\omega^{(20)})$ (green curves) than by $P(\Delta\omega^{(5)})$ (red curves). Further, the number of interactions required to fully converge the distributions illustrates an important distinction between solvent atoms in the first and second solvation shell. In our simulations, roughly 12–15 solvent atoms are found in the first solvation shell. This distinction emerges upon comparing the residuals $P(\Delta\omega^{(10)}) - P(\Delta\omega)$ and $P(\Delta\omega^{(20)}) - P(\Delta\omega)$ (bottom panels). Qualitatively, the residuals $P(\Delta\omega^{(5)}) - P(\Delta\omega)$ and $P(\Delta\omega^{(10)}) - P(\Delta\omega)$ have similar average and maximum values. In contrast, the residuals $P(\Delta\omega^{(20)}) - P(\Delta\omega)$ are indistinguishable from zero within statistical error. Returning to the distributions $P(\Delta\omega^{(10)})$ (blue curves) and $P(\Delta\omega^{(20)})$ (green curves), a closer look shows that the entire distribution $P(\Delta\omega^{(20)})$ lies slightly to the left of $P(\Delta\omega^{(10)})$. The corresponding residuals show that this slight red shift effectively “fills in” the deficit of small red shifts from an excess of small blue shifts. This is because the strongest 10 solute–solvent interactions tend to involve solvent atoms in the first solvation shell, while the next 10 largest solute–solvent interactions tend to involve atoms in the second solvation shell. Long-range attractive interactions from the second solvation shell are predominantly red shifting, and result in a small, constant shift of the entire distribution of line shifts toward the red. This outer solvation shell effect, while small, is necessary to fully converge the distributions of I_2 and ICl line shifts within error.

In summary, consideration of only a single solute–solvent interaction leads to a distribution of line shifts that is too narrow and misses the largest blue shifts. These larger blue shifts are clearly determined by the two or three strongest solute–solvent interactions. Further, a quantitative description of the distributions of I_2 and ICl vibrational line shifts not only requires a description of the solvent atoms that are nearest neighbors to

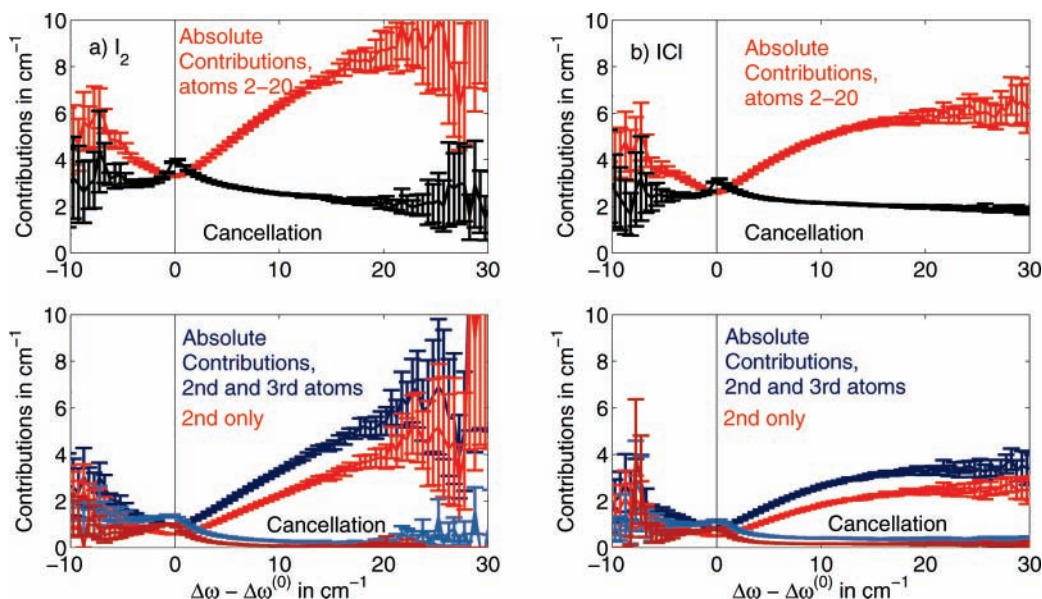


Figure 4. Sum of absolute values of the second through the k th Xe atom contributions to the line shift, as given by eq 11, and cancellation between the top k contributions as defined in eq 12, $k = 2, 3, 20$ vs the sum of solute–solvent contributions to the line shift for (a) I_2 line shifts and (b) ICl line shifts.

the solute but also must account for long-range attractions with the second solvation shell.

The distributions in Figure 2 provide insight into the combined effect on the line shift from a number of solvent atoms. Indirectly, these distributions suggest that the strongest blue shifts come from two or three simultaneous blue-shifting interactions while a single solute–solvent interaction may be largely responsible for the strongest red shifts, and many interactions may cancel to give smaller line shifts. To directly probe the relative magnitudes of the contributions from successive solvent atoms, snapshots from each trajectory were sorted into a histogram based on the instantaneous sum of the solute–solvent contributions, $[\sum_{i=1}^N \Delta V_{01}^{(i)}] / \hbar = \Delta\omega - \Delta\omega^{(0)}$. Within each histogram bin of width 1 cm^{-1} , the average magnitude of each successive solute–solvent contribution was determined:

$$\text{Average Absolute Contribution} = [|\langle \Delta V_{01}^{(\text{Rank } i)} \rangle|] / \hbar \quad (11)$$

for atom ranked $i \leq N - 1$ where $L - \epsilon < \Delta\omega - \Delta\omega^{(0)} < L + \epsilon$ and $\epsilon = 0.5 \text{ cm}^{-1}$. If all of the Xe atom contributions were of the same sign at any given instant, the sum of these averaged, absolute contributions would equal the averaged, absolute value of the total line shift. Accordingly, cancellation between simultaneous red-shifting and blue-shifting interactions is quantified as the difference in magnitude between the sum of absolute and the sum of signed solute–solvent contributions and is averaged within each histogram bin:

$$\text{Average Cancellation} = \frac{1}{\hbar} \left[\left| \left\langle \sum_{i=1}^k |\Delta V_{01}^{(\text{Rank } i)}| \right\rangle \right| - \left| \left\langle \sum_{i=1}^k \Delta V_{01}^{(\text{Rank } i)} \right\rangle \right| \right] \quad (12)$$

for atoms ranked up to $k \leq N - 1$ where $L - \epsilon < \Delta\omega - \Delta\omega^{(0)} < L + \epsilon$ and $\epsilon = 0.5 \text{ cm}^{-1}$.

Absolute magnitudes of the three largest solute–solvent contributions to the line shift are plotted against $\Delta\omega - \Delta\omega^{(0)}$ for I_2 and ICl in Figure 3. Despite large error bars toward the tails of the total frequency distributions, clear trends in the

averages can be identified over an intermediate range. There is nearly a linear correlation between the magnitude of the strongest contributing interaction and that of the total line shift. This trend supports the general conclusion that a single solvent atom plays a major role in determining the line shift at any instant in time. For vibrational red shifts, the strongest solute–solvent contribution is very nearly equal in magnitude to the sum of all contributions. The same is not true of vibrational blue shifts. A linear fit shows that the strongest solute–solvent interaction accounts for $\sim 70\%$ of solute–solvent contributions to I_2 blue shifts, while for ICl, the percentage rises to $\sim 80\%$. The average magnitude of second-ranked contributions also increases with that of the total line shift, although this correlation is not as linear. For I_2 , the second largest absolute contribution is approximately 20% of the sum of solute–solvent contributions; for ICl, the second largest contribution amounts to $\sim 10\text{--}20\%$. These results show that at least two solute–solvent interactions play an important role in line broadening by contributing to stronger blue shifts.

Figure 4 completes the picture by explaining why vibrational red shifts are well described within an “isolated, binary” model of solute–solvent interactions, whereas blue shifts are not. The average magnitude of the cancellation between the 20 largest contributing Xe atoms, defined in eq 12, is shown in Figure 4, as a function of the total I_2 and ICl line shifts. Not surprisingly, cancellation is maximized at total line shifts near zero; these small line shifts naturally result from the nearly complete cancellation of nonzero contributions to the line shift from multiple Xe atoms. At this maximum, the magnitude of the cancellation is nearly 3 cm^{-1} for ICl and $\sim 3.5 \text{ cm}^{-1}$ for I_2 . It is interesting to compare the magnitude that is cancelled out to the total absolute value of the second through 20th contributions. Depending on whether the total line shift is toward the red or blue, this comparison differs qualitatively. When the solute vibration is red shifted, essentially all of the contributions beyond the strongest one are cancelled out on average. When the solute vibration is blue shifted, cancellation decreases to a value that is clearly less than the absolute value of additional solute–solvent contributions. The lower panels show that

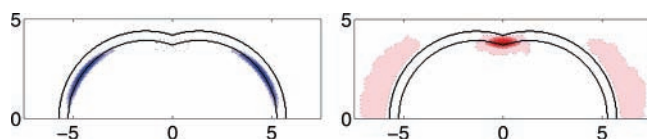


Figure 5. Spatial distribution of the Xe atoms with the largest instantaneous contribution to the I_2 line shift in the following regions of the frequency distribution: left, top 25% of total blue shifts; and right, top 25% of total red shifts. The inner solid black line shows the van der Waals contact radii for the solute atoms and a Xe atom, σ_{I-Xe} , while the outer black line indicates the bottom of the Lennard–Jones potential well, $\sqrt{2}\sigma_{I-Xe}$.

cancellation between the first two atoms drops to a negligible amount when the total line shift is toward the blue. Even the third largest solute–solvent interaction contributes more to blue shifts than to cancellation. For example, when the I_2 vibration is blue shifted by 10 cm^{-1} , the third-ranked solute–solvent interaction alone contributes $\sim 1\text{ cm}^{-1}$; only about 0.2 cm^{-1} of this contribution cancels out on average. From this analysis, a mechanistic picture emerges that describes how a solute vibration is influenced by multiple interactions with nearby solvent atoms. Strong blue-shifting interactions generally occur through a concerted mechanism that involves two or three significant contributors, whereas strong red-shifting interactions generally do not. The following spatial analysis seeks to clarify these two distinct mechanisms.

3.3. Spatial Distribution of Contributing Solvent Atoms.

A complete molecular-level view of the vibrational dynamics should provide a picture that ties the solute vibrational line shift to particular configurations of the solvent around the solute. From the results presented above, it is clear that the strongest few solute–solvent interactions have a profound effect on the line shift. We now turn our attention to the characteristic spatial distributions of these Xe atoms contributing most strongly to the total line shift.

3.3.1. I_2 in Liquid Xe. Two examples of these distributions are presented in Figure 5, which shows filled contour plots of the spatial distribution of the Xe atom with the largest contribution to the line shift. The distributions are plotted in two-dimensional Cartesian coordinates, where the axial symmetry of the diatomic solute has been used to project the data onto the upper half of a plane. Results are shown for two cases: total blue shifts in the largest 25% and total red shifts in the largest 25% (by magnitude). Dotted contour lines are used for clarity, and shades of blue are used to indicate blue-shifting contributions while shades of pink to red are used for red-shifting contributions. In order to place the distributions in context, the I_2 –Xe van der Waals contact radius is shown as is the location of the minimum in the I_2 –Xe Lennard–Jones potential.

The left panel of Figure 5 shows that the top-ranked Xe atom contributors to the top 25% of total blue shifts are centered at the van der Waals contact radius, σ_{I-Xe} ; that is, they are accessing the repulsive part of the I–Xe potential. Further, these Xe atoms are undergoing these repulsive interactions near the ends of the I_2 molecule, indicating that strong blue shifts arise from end-on, collisional interactions. These blue shifts therefore derive from the compression of the vibrating I_2 molecule along the bond axis by the Xe solvent atom. In contrast, spatial distributions for the top-ranked contributors to the top 25% (by magnitude) of total I_2 red shifts are dramatically different, as shown in the right panel of Figure 5. While the distribution for blue shifts exhibits a single kind of interaction, there are two

motifs for the red shifts. The major part of the distribution corresponds to the Xe atom situated in a T-shaped configuration near the center-of-mass of the I_2 molecule. The distribution is centered inside the minimum in the interaction potential and thus represents repulsive I–Xe interactions. The repulsive interactions from this T-shaped geometry serve to push the atoms of the I_2 molecule apart, thereby red shifting the vibrational frequency. A minor component of the distribution involves a Xe atom in an end-on configuration beyond the minimum of the Lennard–Jones potential well. These weaker I_2 –Xe interactions fall on the attractive tail of the potential, indicating that the Xe atom serves to pull the I_2 molecule apart in the direction of the bond axis. Although a smaller part of the distribution than the repulsive interactions, to be part of this distribution, they must be (at times) the most important single interaction. Clearly, the Xe atom contributing the most to a line shift can be in any one of these three types of locations with respect to the I_2 solute.

As discussed above, the line shift cannot generally be attributed to a single Xe solvent atom. Thus, it is instructive to look at the spatial distributions for the Xe atoms that make the second and third largest contributions to the total line shift. These are shown in Figure 6, for different parts of the I_2 instantaneous vibrational frequency distribution. Specifically, the blue-shifted side of the frequency distribution has been divided up into four parts, and spatial distributions are shown for the first, or top, quartile of blue-shifted frequencies and the fourth quartile (smallest blue shifts); analogous results are shown for the red-shifted side of the frequency distribution. Recall that the three largest Xe atom contributions to the line shift can either cooperate to enhance the total line shift or cancel to decrease the total line shift.

As was seen from Figure 2, large blue shifts generally result from the additive contributions of at least two Xe atoms interacting simultaneously. This is further illustrated by the spatial distributions of the three largest-contributing Xe atoms, which are plotted in the top row of Figure 6 for the largest 25% of the blue shifts. These spatial distributions show that the second strongest contribution is nearly always from a repulsive, end-on I–Xe interaction. The repulsive interaction arises from a Xe atom that is slightly further out on the repulsive wall than the largest-contributing Xe atom and also angled slightly closer to the center of the I_2 molecule. There are two minor components of the distribution that correspond to red-shifting interactions, a T-shaped geometry with the Xe atom near the I_2 center-of-mass and end-on configurations with the Xe atom in the attractive region of the I–Xe Lennard–Jones potential. The spatial distribution for the third strongest contributing Xe atom has the same general features as that for the second. The primary differences are that the repulsive, end-on geometries that lead to blue shifting are less dominant, correspond to Xe atoms slightly further out on the repulsive wall, and are angled slightly further from the bond axis. These observations are consistent with the truncated frequency distributions shown in Figure 2a for the top three contributing Xe atoms.

Figure 2 also shows that the effect of multiple I_2 –Xe interactions on red shifts is less dramatic. The spatial distributions for the three largest-contributing Xe atoms giving rise to the largest 25% of red shifts are shown in the bottom row of Figure 6. These distributions show that the second- and third-ranked contributions to the line shift are predominantly red-shifting, with either attractive, end-on geometries or T-shaped, repulsive geometries. The small percentage of Xe atoms found in repulsive, off-center geometries results only in minor blue-

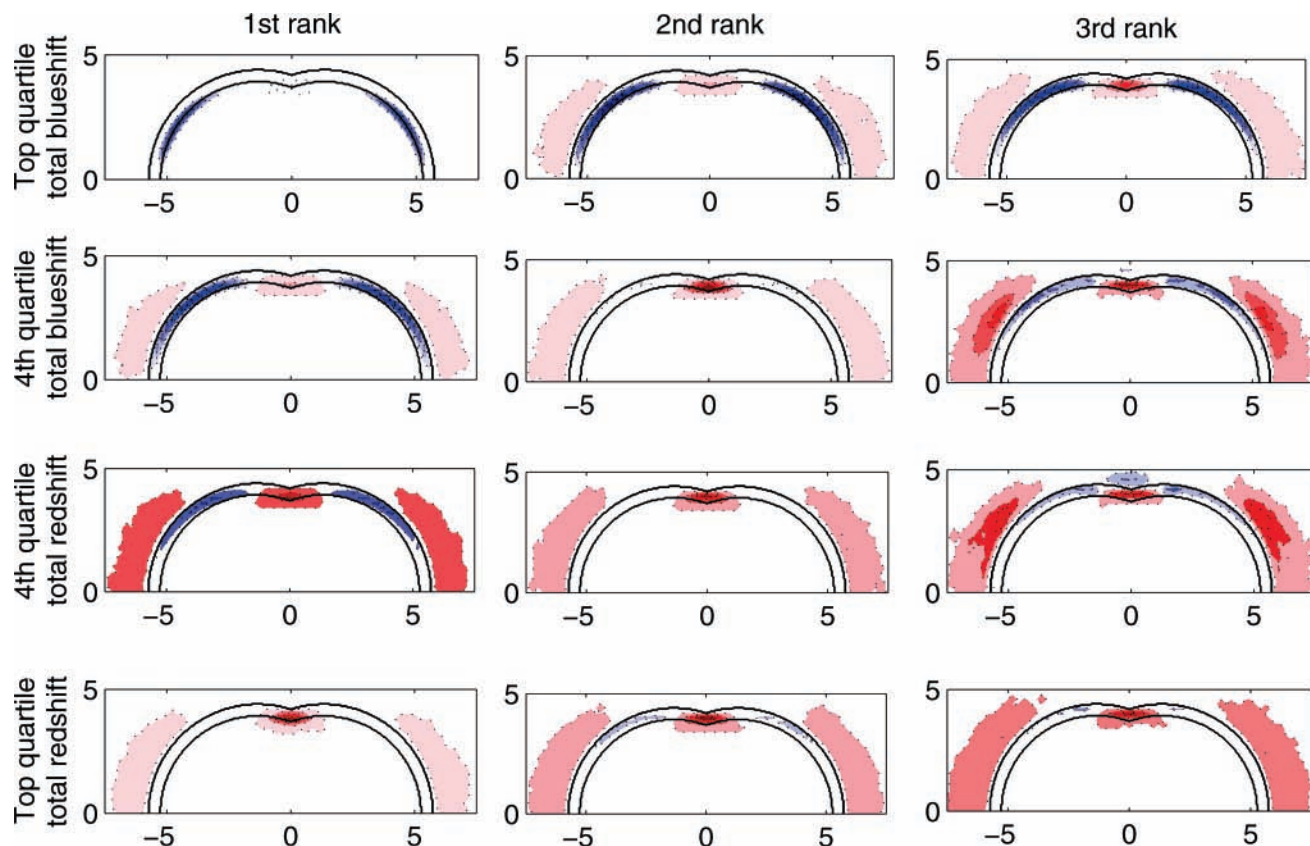


Figure 6. Spatial distributions for solvent atoms contributing to I_2 line shifts in the following regions of the frequency distribution: (a) top 25% of total blue shifts, (b) bottom 25% of total blue shifts, (c) bottom 25% of total red shifts, and (d) top 25% of total red shifts. Spatial distributions are given for the top three contributing solute–solvent interactions.

shifting contributions. These distributions indicate that strong I_2 red shifts occur only when strong blue-shifting interactions are not present.

Smaller total line shifts arise when red-shifting and blue-shifting interactions of a similar magnitude occur simultaneously. The middle two rows of Figure 6 display the spatial distributions of the three Xe atoms that contribute the most to the total line shift when that line shift is in the bottom 25% of blue shifts or the bottom 25% of red shifts. In both cases, that is, independent of whether the total line shift is blue or red, the strongest I_2 –Xe interaction may be either blue-shifting (repulsive, end-on) or red-shifting (T-shaped or attractive, end-on). The spatial distribution for small blue shifts is weighted more to repulsive, end-on configurations, while the distribution for small red shifts is weighted more to T-shaped and attractive, end-on configurations. Interestingly, for both small blue shifts and small red shifts, the second-largest Xe atom contribution is almost always a red-shifting one. The spatial distribution for the third-ranked Xe atom contains significant components from all three types of interactions and thus may be either weakly red shifting or weakly blue shifting. However, in the distribution for the bottom 25% of red shifts, a new, fourth motif arises in which the Xe atom is in a T-shaped geometry but in the attractive part of the potential. Thus, it causes a blue shift by pulling together the two atoms of the I_2 molecule. Taken together, these spatial distributions illustrate that when there are no strong collisional interactions, a collection of smaller contributions combine either constructively or destructively to give small red shifts or blue shifts.

3.3.2. ICl in Liquid Xe. Spatial distributions also provide detailed insight into the correlation between Xe atom positions

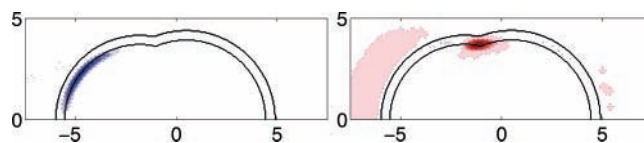


Figure 7. Same as Figure 5 but for the ICl solute.

and vibrational line shift contributions for the asymmetric molecule ICl, providing an important comparison with I_2 . The spatial distributions for Xe atoms that contribute strongly to the ICl total line shift are shown in Figures 7 and 8. Figure 7 shows distributions for the Xe atom with the largest contribution when the ICl blue shift is in the top 25% of observed blue shifts and the analogous distribution for the largest 25% of red shifts. Most notably, the strongest contributing Xe atom is found only in an end-on configuration on the Cl side of the molecule when ICl is strongly blue-shifted. As with I_2 , these end-on configurations feature Xe on the repulsive wall of the Cl–Xe potential, compressing the diatomic bond. Similarly, attractive, end-on interactions between ICl and Xe atoms beyond the potential well minimum, which can at times be the strongest red-shifting interaction, are also concentrated at the Cl end of the solute. Just as with the I_2 solute, side-on (T-shaped) geometries are the dominant configuration giving rise to strong red shifts. The major difference between the I_2 and ICl solutes is the possibility of interactions between the solvent atoms and the lighter and smaller Cl atom. Figure 7 identifies these Cl–Xe interactions as top contributors to the strongest vibrational line shifts.

Figure 8 provides a fuller picture of how Xe atom configurations relative to the ICl solute correspond to larger and smaller blue shifts and red shifts. The first row of Figure 8 shows the

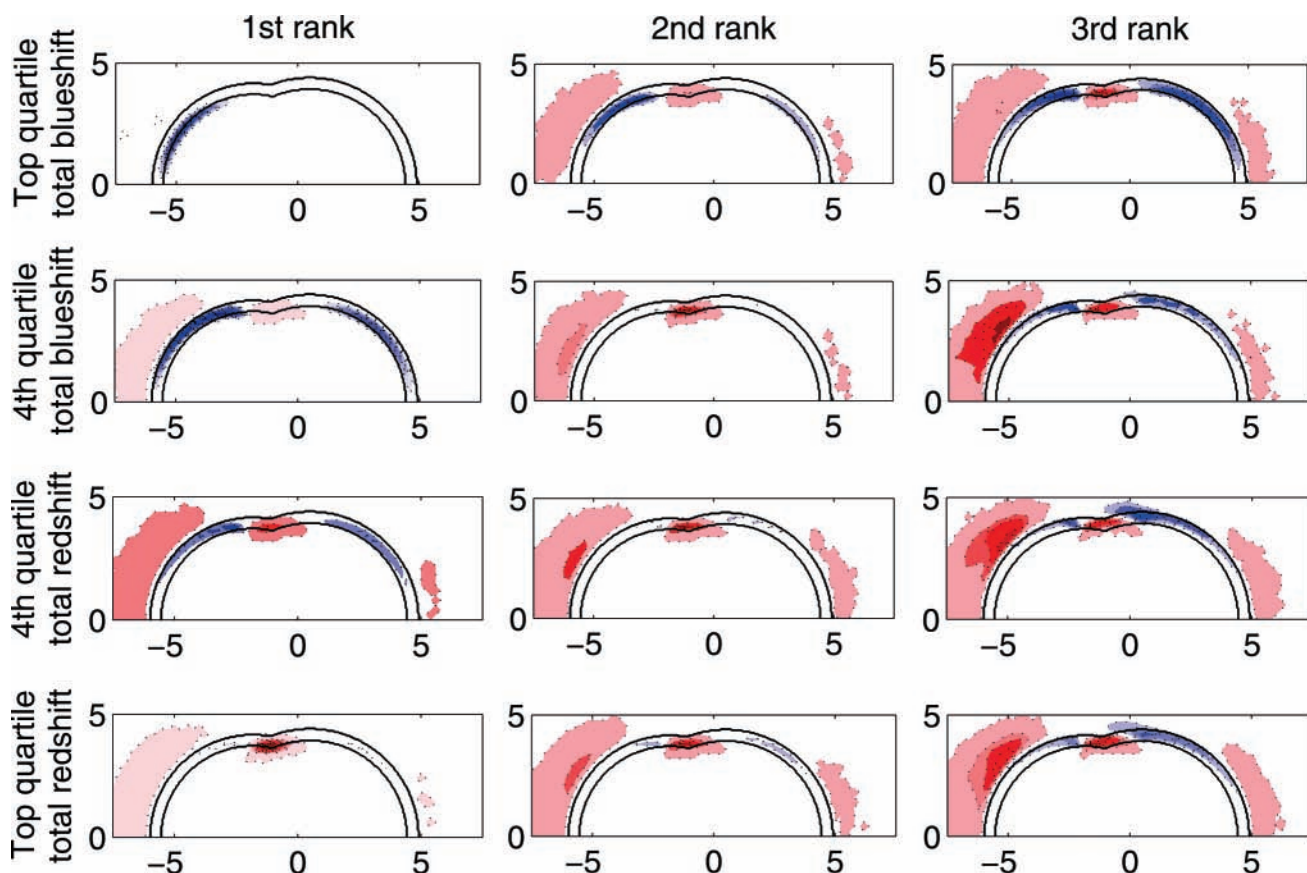


Figure 8. Same as Figure 6 but for the ICl solute.

spatial distributions of the Xe atoms with the three largest contributions to the line shift when the total line shift is in the largest 25% of blue shifts. The distributions for the Xe atoms with the second and third largest contributions to these large blue shifts are in one sense qualitatively similar to those for I_2 . Namely, the weaker interactions involve Xe atoms further down the repulsive wall, and some likelihood of red-shifting interactions (both T-shaped and end-on) is observed. However, the asymmetry is significant, showing that I–Xe interactions have a weaker blue-shifting effect on the ICl vibration. The spatial distributions for the three largest contributors to the line shift are plotted for large total red shifts in the bottom row of Figure 8. These show that large red shifts arise primarily from T-shaped configurations with Xe on the repulsive wall of the ICl–Xe potential and, to a lesser extent, with Xe atoms in attractive, end-on interactions with the Cl end of the molecule. Attractive, end-on configurations with Xe on the I side of the molecule contribute more weakly as second- or third-ranked interactions, along with weakly blue-shifting configurations in which Xe is just within the potential minimum, and is angled far from the bond axis, closer to the I end of ICl, or both. Small total red shifts or blue shifts, as shown in the middle two rows of Figure 8, arise from a combination of several weaker interactions in the absence of stronger collisional contributions. Namely, the Xe atom making the strongest contribution can be either red shifting or blue shifting if the total line shift is small. As with I_2 , the Xe atom with the second-largest contribution to the line shift is almost always red shifting, while the third-ranked Xe atom can have either a red shifting or a blue shifting effect. Hence, the primary difference between I_2 and ICl is that, for the latter, the Xe atoms interact more effectively with the Cl side of the molecule.

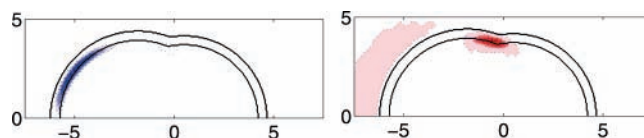


Figure 9. Spatial distribution of solvent atoms with the top contribution to fictitious solute line shifts in the following regions of the distribution: (a) top 25% of total blue shifts, and (b) top 25% of total red shifts. Outlines depict σ and $\sqrt{2}\sigma$ for this fictitious solute molecule, as in previous figures. Solute masses are the same as those used for ICl, but the potential parameters of the atoms are reversed in the fictitious solute. See text for further discussion.

The comparison of the spatial distributions for I_2 and ICl raises the questions: Why do the Xe atoms shift the vibrational frequency most effectively through interaction with the Cl atom? Is this an effect of the mass or the potential? This issue can be addressed by examining the spatial distributions for the Xe atoms around one of the fictitious solute molecules discussed above, for which the potential parameters of I and Cl are reversed. In Figure 9 the distributions for the Xe atom with the largest contribution to the line shift are shown for this fictitious solute. Distributions are plotted for the top 25% of blue shifts and the top 25% of red shifts, analogous to Figures 5 and 7. Just as with the ICl molecule, the strongest blue-shifting interactions involve a Xe atom in a repulsive, end-on configuration at the lighter (but now larger) end of the fictitious solute. Similarly, attractive, end-on configurations that are top contributors to stronger red shifts are focused near the lighter end. In both cases, the distributions are shifted relative to ICl in accord with the new van der Waals radii. Because the lighter atom is larger than Cl, end-on interactions are distributed over a broader spatial

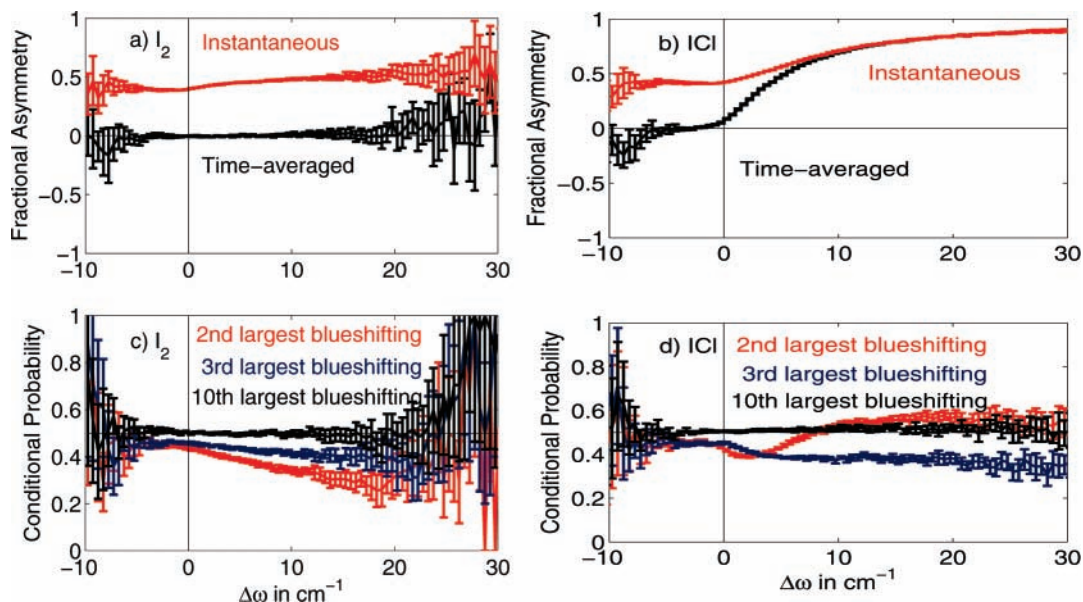


Figure 10. Top panels: averaged and instantaneous asymmetry of all blue shifting contributions for (a) I_2 and (b) ICI. The conditional probability that the k th blue-shifting solute–solvent interaction is on the same side as the strongest blue-shifting interaction, given the total line shifts on the abscissa for (c) I_2 and (d) ICI.

region. This explains why strong blue shifts are even more prevalent for the fictitious solute than for ICI. Although not shown here (see Supporting Information), distributions of the second and third strongest contributing solvent atoms for blue shifts and red shifts of this fictitious solute are qualitatively the same as those of ICI shown in Figure 7. The top two contributions to strong blue shifts are mostly blue-shifting interactions and are distributed preferentially toward the lighter end; also, red-shifting attractive interactions are distributed preferentially toward the lighter end. For both ICI and the fictitious solute, interactions with the lighter atom clearly lead to more substantial changes in the solute vibrational frequency. This mechanism is consistent with the idea that strong blue shifts are more prevalent for ICI than for I_2 because Cl is lighter.

3.4. Instantaneous and Time-Averaged Asymmetry. The analysis presented in section 3.2 showed that typically one Xe atom is responsible for a majority of the vibrational line shift but the total blue shift is sensitive to contributions from multiple solvent atoms. In section 3.3, it was further demonstrated that strong blue-shifting contributions are associated with solvent atoms near the ends of the solute molecule. We now attempt to clarify whether cooperative blue-shifting contributions come from the same or opposite ends of the solute molecule. For each 1 cm^{-1} wide histogram bin of the total line shift distribution, a dividing plane is placed between the “left” and the “right” atoms at the intersection of the van der Waals radii of the two solute atoms. The instantaneous asymmetry in blue-shifting contributions is then defined:

$$\text{Instantaneous asymmetry} = \frac{\left\langle \left| \left(\sum_j \Delta\omega_j^{\text{blue, left}} \right) - \left(\sum_k \Delta\omega_k^{\text{blue, right}} \right) \right| \right\rangle_L}{\left\langle \sum_{j=2}^N \Delta\omega_j^{\text{blue}} \right\rangle_L} \quad (13)$$

where $L - \epsilon < \Delta\omega < L + \epsilon$, $\epsilon = 0.5 \text{ cm}^{-1}$, and $\Delta\omega_j = \Delta V_{01}^j / \hbar$. In the limit that a single, strong blue-shifting interaction accounts for the total line shift, instantaneous asymmetry should be unity

at all times, regardless of the inherent spatial symmetry of the solute molecule. Time-averaged asymmetry was also evaluated, on the basis of the signed differences between contributions at the left and right end of the solute:

$$\text{Time-averaged asymmetry} = \frac{\left\langle \left(\sum_j \Delta\omega_j^{\text{blue, left}} \right) - \left(\sum_k \Delta\omega_k^{\text{blue, right}} \right) \right\rangle_L}{\left\langle \sum_{j=2}^N \Delta\omega_j^{\text{blue}} \right\rangle_L} \quad (14)$$

where $L - \epsilon < \Delta\omega < L + \epsilon$, $\epsilon = 0.5 \text{ cm}^{-1}$, and $\Delta\omega_j = \Delta V_{01}^j / \hbar$. Both are fractional measures; time-averaged asymmetry can vary between -1 and 1 while instantaneous asymmetry is always positive and varies between 0 and 1 . Another metric that also varies between 0 and 1 is the conditional probability that a given blue-shifting contribution comes from the same side as the strongest blue-shifting interaction; see Figure 10. When several blue-shifting contributions are important, this can provide clues as to the instantaneous configuration of these solvent atoms.

The calculated instantaneous and time-averaged asymmetries in the blue-shifting contributions as a function of the total line shift are shown for the symmetric I_2 solute in Figure 10a. As expected, the time-averaged asymmetry is zero for all values of the total vibrational line shift; this is merely a confirmation that we have sufficient statistical sampling. The instantaneous asymmetry is nonzero, but remains about the same (approximately 0.5) over the whole range of line shifts. This is surprising, given that the strongest I_2 –solvent interaction contributes $\sim 65\%$ to I_2 blue shifts. The probabilities in Figure 10c show that when the total line shift is toward the blue, the second- and third-largest blue-shifting contributions are more likely to come from solute atoms on the opposite end of I_2 . These help to compensate for the disproportionate strength of the largest blue-shifting contribution, keeping the instantaneous asymmetry to about 0.5 as shown in the top panel.

For the inherently asymmetric ICI molecule (Figure 10b), the time-averaged asymmetry of the blue-shifting contributions is

nonzero and varies with the total line shift. Interestingly, this time-averaged asymmetry is approximately -0.5 to -0.25 (toward the heavy end of the ICl solute) when the total line shift is toward the red, but it climbs sharply when the line shift is toward the blue and eventually matches the instantaneous asymmetry. This reflects the increased magnitude of blue-shifting contributions near the lighter Cl end of ICl. Instantaneous asymmetry is near 0.5 when the vibrational frequency is red-shifted, but predictably increases with the magnitude of overall blue shifts. Also, because the second largest blue-shifting contribution increases with the magnitude of the total blue shift, and because of the preference for stronger interactions toward the lighter end of ICl, the two largest contributions are more likely to come from the same side of the solute than is the case for I_2 . For large blue shifts, the second contributions are nearly equally likely to come from either side of ICl.⁵⁴ As shown in Figure 10d, third-ranked blue-shifting contributions are more likely to come from the opposite, heavier end of ICl, regardless of the total line shift.

Asymmetry is one way of relating the total line shift to the configuration of blue shifting solvent atoms around the solute. In the case of I_2 , the second- and third-ranked blue-shifting interactions are more likely to occur on the side opposite from the strongest one. An instantaneous asymmetry of about 0.5 is maintained, regardless of the line shift. For ICl, the larger blue-shifting interactions occur near the lighter end of the solute. In this case, both instantaneous and time-averaged asymmetry increase with larger blue shifts, and they are identical for blue shifts larger than $\sim 10\text{ cm}^{-1}$.

4. Conclusion

Mixed quantum-classical simulations have been analyzed to provide a mechanistic explanation for spectral diffusion that gives rise to vibrational frequency distributions for I_2 and ICl in liquid Xe. Spectral diffusion has been explained in terms of instantaneous solute-solvent interactions. Interactions with all solvent atoms in the first and second solvation shell are required to quantitatively reproduce the line shift distribution. However, the qualitative features are captured by the contributions from one solvent atom for the red shifts and two or three solvent atoms for the blue shifts. Strong blue shifts arise as a result of repulsive interactions with solvent atoms near the ends of the solute. These occur when the solute is compressed by solvent atoms along the bond axis. While there is always one strongest solute-solvent interaction, there are also strong repulsive interactions with one or two additional solvent atoms near the ends of the solute. For strong ($10\text{--}20\text{ cm}^{-1}$) blue shifts, the second most important solute-solvent interaction accounts for an average of $\sim 10\text{--}20\%$ of the line shift. For I_2 , these additional interactions are more likely to involve solvent atoms on the opposite end that can be thought of as effectively holding the solute in place. Strong red shifts arise as a result of repulsive interactions with a solvent atom positioned near the center-of-mass of the solute and perpendicular to the bond axis in a T-shaped geometry. This interaction pushes the solute atoms apart, lengthening the bond axis. Other solute-solvent interactions effectively cancel out and do not significantly change the magnitude of the line shift. Strong red shifts occur when there are no solvent atoms sufficiently close to the ends of the solute to compress the bond axis. These simulations suggest that an isolated binary collision model is not sufficient to explain the distribution of vibrational line shifts. Only the red shifts can be viewed qualitatively in terms of a single solute-solvent interaction because of the nearly wholesale cancellation of the

smaller contributing red shifts. Additionally, the sign and magnitude of each solute-solvent contribution to the line shift is strongly dependent on both distance and the interaction angle (perpendicular or end-on).

The asymmetry of the ICl molecule offers an interesting point of contrast. Solvent atoms that are closer to the lighter Cl atom have a larger impact on vibrational line shifts than those that are near the heavier I atom. Simulations with a fictitious solute confirm that this enhancement is due to the lighter mass of Cl, not the atom-dependent potential parameters. Because the strongest end-on interactions are blue shifting, the most noticeable effect is the increase in strong blue shifts. This explains why the frequency distribution for ICl includes more strong blue shifts than that of I_2 in the same liquid Xe environment.

For a quantitatively accurate model of the entire I_2 or ICl frequency distribution, attractive interactions with solvent atoms in the second solvation shell must also be taken into account. Solvent atoms that are further out on the attractive tail of the potential have a smaller but opposite effect: end-on interactions pull the solute atoms apart along the bond axis, and T-shaped interactions pull them together. In these simulations, ~ 20 solute-solvent interactions were needed to reproduce the distribution of line shifts within a 95% confidence interval.

Some of these conclusions bear a resemblance to the behavior of I_2 and ICl in clusters with one or more rare gas atoms. Stable van der Waals complexes are known to form with a single rare gas atom in both linear and T-shaped geometries, and their vibrational relaxation has been studied in detail by experiment and theory.⁵⁵⁻⁵⁸ However, these clusters likely do not access the more repulsive regions of the ground state potential that appear to influence frequency shifts in the condensed phase. An interesting comparison arises with I_2^- vibrational line shifts in clusters of the form $I_2^-(Ar)_n$, which are more tightly bound because of the negative charge.⁵⁹ A slight red shift was reported for $I_2^-(Ar)_6$ clusters with Ar arranged around the center of the I_2^- bond axis, and the frequency was blue shifted incrementally as Ar atoms were added near the ends of I_2^- . Our analysis of condensed-phase frequency shifts is consistent with the physical picture from these ion-cluster experiments, which both indicate that the relevant solute-solvent interactions are primarily repulsive.⁵⁹

The present work focuses on spectral diffusion in bulk Xe, a simple model liquid. Further work is necessary to extend this view to more realistic, polar solvents; more accurate modeling of the interactions may also be required.⁶⁰ By directly relating the vibrational frequency distribution to the liquid structure, this approach will be useful in future studies to explain the effects of confinement on vibrational spectra. In a confined liquid, significant anisotropy may arise because of solvent packing as well as solute-wall interactions. If repulsive interactions act along the solute vibration, a stronger blue-shifting effect would be expected by analogy to the present results, while red shifts would be expected for interactions perpendicular to the bond. Another layer of complexity is added by possible contributions from long-range attractive forces within a polar solvent.⁶¹

While this paper describes the molecular-level mechanisms of vibrational spectral shifts for the simple I_2 in Xe system, the approaches are readily applicable to more complex solutes and solvents. For example, in polar systems contributions to frequency shifts can be assigned not only to individual solvent molecules/atoms but also to Lennard-Jones or Coulombic interactions. Further, we have previously demonstrated that analogous mechanistic information can be extracted for vibrational energy relaxation through the nonadiabatic coupling.^{31,29}

We are currently applying these approaches to complex heterogeneous systems, specifically, solutes dissolved in liquids that are confined on nanometer length scales, where the effect of the interface on the vibrational spectra and relaxation times is an important issue.

Acknowledgment. The authors thank Dr. Tolga S. Gulmen for many useful discussions. This work was supported by the National Science Foundation (Grant CHE-0518290).

Supporting Information Available: Non-additive contributions to the line shift and additional spatial distributions for two fictitious solutes, one with I₂ masses and ICl potentials and the other with ICl masses and switched ICl potentials. This material is available free of charge via the Internet at <http://pubs.acs.org>.

References and Notes

- Czeslik, C.; Kim, Y. J.; Jonas, J. *J. Chem. Phys.* **1999**, *111*, 9739–9742.
- Lee, Y. T.; Wallen, S. L.; Jonas, J. *J. Phys. Chem.* **1992**, *96*, 7161–7164.
- Czeslik, C.; Kim, Y. J.; Jonas, J. *J. Raman Spectrosc.* **2000**, *31*, 571–575.
- Yi, J.; Jonas, J. *J. Phys. Chem.* **1996**, *100*, 16789–16793.
- Czeslik, C.; Kim, Y. J.; Jonas, J. *J. Phys. Chem. A* **2000**, *104* (P7), 103–106.
- Tominaga, K.; Okuno, H.; Maekawa, H.; Tomonaga, T.; Loughnane, B. J.; Scodinu, A.; Fourkas, J. T. In *Liquid Dynamics: Experiment, Simulation, and Theory*; Fourkas, J. T., Ed.; American Chemical Society: Washington, D.C., 2002; Vol. 820, pp 160–168.
- Nikiel, L.; Hopkins, B.; Zerda, T. W. *J. Phys. Chem.* **1990**, *94*, 7458–7464.
- Hoang, G. C. *J. Korean Phys. Soc.* **2002**, *40*, 224–231.
- Kamble, V. S.; Gupta, N. M. *J. Phys. Chem. B* **2000**, *104*, 4588–4592.
- Sahasrabudhe, A.; Mitra, S.; Tripathi, A. K.; Mukhopadhyay, R.; Gupta, N. M. *Phys. Chem. Chem. Phys.* **2003**, *5*, 3066–3075.
- Riter, R. E.; Undiks, E. P.; Kimmel, J. R.; Levinger, N. E. *J. Phys. Chem. B* **1998**, *102*, 7931–7938.
- Riter, R. E.; Undiks, E. P.; Levinger, N. E. *J. Am. Chem. Soc.* **1998**, *120*, 6062–6067.
- Venables, D. S.; Huang, K.; Schmuttenmaer, C. A. *J. Phys. Chem. B* **2001**, *105*, 9132–9138.
- Zhong, Q.; Steinhurst, D. A.; Carpenter, E. E.; Owrutsky, J. C. *Langmuir* **2002**, *18*, 7401–7408.
- Zhong, Q.; Baronavski, A. P.; Owrutsky, J. C. *J. Chem. Phys.* **2003**, *118*, 7074–7080.
- Zhong, Q.; Baronavski, A. P.; Owrutsky, J. C. *J. Chem. Phys.* **2003**, *119*, 9171–9177.
- Sando, G. M.; Dahl, K.; Owrutsky, J. C. *J. Phys. Chem. A* **2004**, *108*, 11209–11217.
- Sando, G. M.; Dahl, K.; Zhong, Q.; Owrutsky, J. C. *J. Phys. Chem. A* **2005**, *109*, 5788–5792.
- Sando, G. M.; Dahl, K.; Owrutsky, J. C. *Chem. Phys. Lett.* **2006**, *418*, 402–407.
- Horikawa, S.; Itoh, H.; Tabata, J.; Kawamura, K.; Hondoh, T. *J. Phys. Chem. B* **1997**, *101*, 6290–6292.
- van Klaveren, E. P.; Michels, J. P. J.; Schouten, J. A.; Klug, D. D.; Tse, J. S. *J. Chem. Phys.* **2002**, *117*, 6637–6645.
- Li, S.; Shepherd, T. D.; Thompson, W. H. *J. Phys. Chem. A* **2004**, *108*, 7347–7355.
- Korb, J.-P.; Delville, A.; Xu, S.; Demeulenaere, G.; Costa, P.; Jonas, J. *J. Chem. Phys.* **1994**, *101*, 7074–7081.
- Wallen, S. L.; Nikiel, L.; Yi, J.; Jonas, J. *J. Phys. Chem.* **1995**, *99*, 15421–15427.
- Kalampounias, A. G.; Kirillov, S. A.; Steffen, W.; Yannopoulos, S. N. *J. Mol. Struct.* **2003**, *651–653*, 475–483.
- Kalampounias, A. G.; Yannopoulos, S. N.; Steffen, W.; Kirillova, L. I.; Kirillov, S. A. *J. Chem. Phys.* **2003**, *118*, 8340–8349.
- Thompson, W. H. *J. Chem. Phys.* **2003**, *118*, 1059–1067.
- Rey, R.; Hynes, J. T. *J. Chem. Phys.* **1998**, *108*, 142–153.
- Li, S.; Thompson, W. H. *Chem. Phys. Lett.* **2004**, *383*, 326–331.
- Fecko, C. J.; Eaves, J. D.; Loparo, J. J.; Tokmakoff, A.; Geissler, P. L. *Science* **2003**, *301*, 1698–1702.
- Li, S.; Thompson, W. H. *J. Phys. Chem. A* **2003**, *107*, 8696–8704.
- Paige, M. E.; Harris, C. B. *Chem. Phys.* **1990**, *149*, 37–62.
- Paige, M. E.; Russell, D. J.; Harris, C. B. *J. Chem. Phys.* **1986**, *85*, 3699–3700.
- Brown, J. K.; Harris, C. B.; Tully, J. C. *J. Chem. Phys.* **1988**, *89*, 6687–6696.
- Egorov, S. A.; Skinner, J. L. *J. Chem. Phys.* **1996**, *105*, 7047–7058.
- Miller, D. W.; Adelman, S. A. *J. Chem. Phys.* **2002**, *117*, 2672–2687.
- Adelman, S. A.; Muralidhar, R.; Stote, R. H. *J. Chem. Phys.* **1991**, *95*, 2738–2751.
- Stote, R. H.; Adelman, S. A. *J. Chem. Phys.* **1988**, *88*, 4415–4420.
- Nesbitt, D. J.; Hynes, J. T. *Chem. Phys. Lett.* **1981**, *82*, 252–254.
- Nesbitt, D. J.; Hynes, J. T. *J. Chem. Phys.* **1982**, *76*, 6002–6014.
- Larsen, R. E.; Stratt, R. M. *J. Chem. Phys.* **1999**, *110*, 1036–1052.
- Bastida, A.; Cruz, C.; Zúñiga, J.; Requena, A.; Miguel, B. *J. Chem. Phys.* **2004**, *121*, 10611–10622.
- Bastida, A.; Cruz, C.; Zúñiga, J.; Requena, A.; Miguel, B. *Chem. Phys. Lett.* **2006**, *417*, 53–57.
- Sato, M.; Okazaki, S. *J. Chem. Phys.* **2005**, *123*, 124508.
- Litovitz, T. A. *J. Chem. Phys.* **1957**, *26*, 469–473.
- Davis, P. K.; Oppenheim, I. J. *Chem. Phys.* **1972**, *57*, 505–517.
- Fischer, R. F.; Laubereau, A. *Chem. Phys. Lett.* **1975**, *35*, 6–12.
- Oxtoby, D. W. *Mol. Phys.* **1977**, *34*, 987–994.
- Allen, M. P.; Tildesley, D. J. *Computer Simulation of Liquids*; Oxford University Press: New York, 1987.
- Herzberg, G. *Molecular Spectra and Molecular Structure*, Vol. 1, 2nd ed.; Krieger Publishing Company: Malabar, FL, 1989.
- Shoemaker, D. P.; Garland, C. W.; Nibler, J. W. *Experiments in Physical Chemistry*, 5th ed.; McGraw-Hill: New York, 1989.
- Abramowitz, M.; Stegun, I. A. *Handbook of Mathematical Functions: with Formulas, Graphs, and Mathematical Tables*, 9th ed.; Dover Publications: Mineola, NY, 1970.
- $\Delta\omega^{(1)} = 0$ for timesteps in which the strongest solute–solvent interaction $\Delta V_{01}^{(1)}/\hbar$ exactly cancels the remaining terms $\{\{\Delta T_{01}^r - \Delta T_{01}^c(\text{gas})\} + \Delta T_{01}^c + \{\hat{V}_{01}^{AB}(r) - \hat{V}_{01}^{AB}(r)(\text{gas})\}\}/\hbar$.
- In Figure 8, the spatial distribution for the second strongest contribution to large blue shifts appears concentrated toward the Cl end of the solute. Contributions from the other end of the solute are distributed more diffusely in space and are therefore less visually apparent. However, integration of the spatial distribution shows that the second largest contribution is almost equally likely to come from either end of ICl.
- Rohrbacher, A.; Halberstadt, N.; Janda, K. C. *Annu. Rev. Phys. Chem.* **2000**, *51*, 405–433.
- Buchachenko, A.; Halberstadt, N.; Lepetit, B.; Roncero, O. *Int. Rev. Phys. Chem.* **2003**, *22*, 153–202.
- McCoy, A. B.; Darr, J. P.; Boucher, D. S.; Winter, P. R.; Bradke, M. D.; Loomis, R. A. *J. Chem. Phys.* **2004**, *120*, 2677–2685.
- Ray, S. E.; McCoy, A. B.; Glennon, J. J.; Darr, J. P.; Fesser, E. J.; Lancaster, J. R.; Loomis, R. A. *J. Chem. Phys.* **2006**, *125*, 164314.
- Zanni, M. T.; Greenblatt, B. J.; Neumark, D. M. *J. Chem. Phys.* **1998**, *109*, 9648–9651.
- Li, S.; Schmidt, J. R.; Corcelli, S. A.; Lawrence, C. P.; Skinner, J. L. *J. Chem. Phys.* **2006**, *124*, 204110.
- Ladanyi, B. M.; Stratt, R. M. *J. Chem. Phys.* **1999**, *111*, 2008–2018.